

# Effects of anisotropy on the geometry of tracer particle trajectories in turbulent flows

Yasmin Hengster<sup>a,\*</sup>, Martin Lellep<sup>b</sup>, Julian Weigel<sup>c</sup>, Matthew Bross<sup>d,e</sup>,  
Johannes Bosbach<sup>f</sup>, Daniel Schanz<sup>f</sup>, Andreas Schröder<sup>f,g</sup>, Florian Huhn<sup>f</sup>,  
Matteo Novara<sup>f</sup>, Daniel Garaboa Paz<sup>h</sup>, Christian Kähler<sup>e</sup>, Moritz Linkmann<sup>a,\*</sup>

<sup>a</sup>*School of Mathematics and Maxwell Institute for Mathematical Science, University of Edinburgh, Mayfield Rd, Edinburgh, EH9 3FD, United Kingdom*

<sup>b</sup>*SUPA, School of Physics and Astronomy, University of Edinburgh, Peter Guthrie Tait Rd, EH9 3FD, Edinburgh, United Kingdom*

<sup>c</sup>*Department for Physics and Astronomy, University of Heidelberg, D-69120, Heidelberg, Germany*

<sup>d</sup>*Fluids Research Department, Applied Research Laboratory (ARL), Pennsylvania State University, State College PA, United States*

<sup>e</sup>*Institute of Fluid Mechanics and Aerodynamics, Universität der Bundeswehr München, Neubiberg, Germany*

<sup>f</sup>*German Aerospace Center (DLR), Institute of Aerodynamics and Flow Technology, Göttingen, Germany*

<sup>g</sup>*Brandenburgische Technische Universität (BTU), Cottbus-Senftenberg, Germany*

<sup>h</sup>*Group of Non-linear Physics, University of Santiago de Compostela, Spain*

---

## Abstract

Using curvature and torsion to describe Lagrangian trajectories gives a full description of these as well as an insight into small and large time scales as temporal derivatives up to order 3 are involved. One might expect that the statistics of these properties depend on the geometry of the flow. Therefore, we calculated curvature and torsion probability density functions (PDFs) of experimental Lagrangian trajectories processed using the Shake-the-Box algorithm of turbulent von Kármán flow, Rayleigh-Bénard convection and a zero-pressure-gradient boundary layer over a flat plate. The results for the von Kármán flow compare well with experimental results for the curvature PDF and numerical simulation of homogeneous and isotropic turbulence for the torsion PDF. For the experimental Rayleigh-Bénard convection, the power law tails found agree with those measured for von Kármán flow. Results for the logarithmic layer within the boundary layer differ slightly, we give some potential explanation below. To detect and quantify the effect of anisotropy either resulting from a mean flow or large-scale coherent motions on the geometry of tracer particle trajectories, we introduce the curvature vector. We connect its statistics with those of velocity fluctuations and demonstrate that strong large-scale motion in a given spatial direction results in meandering rather than helical trajectories.

---



---

\*Corresponding authors

## 1. Introduction

An important feature of turbulent flows in nature and engineering applications is large-scale spatio-temporal coherence, more precisely, the presence of persistent large-scale structures. Such *turbulent superstructures* occur in turbulent boundary layers in the laboratory [1, 2, 3, 4] or the atmosphere [5], and also in Rayleigh-Bénard convection [6, 7, 8, 9], for instance. They influence mixing and extreme events and, at least in case of turbulent boundary layers, contribute significantly to momentum exchange and kinetic energy of the flow [10, 11] and to the Reynolds stress [12, 3]. One particular question that is of interest from a fundamental and from a turbulence modelling perspective is the connection between turbulent superstructures and extreme small-scale velocity fluctuations [13, 14], in particular near a solid boundary. Unusually high values of torsion and curvature in tracer particle trajectories indicate the presence of intense small-scale vortices. These can usually not be resolved in numerical simulations at parameters relevant in industrial applications or atmospheric physics, that is, their effect needs to be incorporated into turbulence models. There is no doubt that large-scale spatio-temporally coherent structures influence the motion of Lagrangian particle trajectories, and presumably the statistics of instantaneous curvature and torsion thereof. Curvature is a multi-scale observable in the sense that connects velocity and acceleration, hence its statistics may contain information regarding the effect of large-scale dynamics on the small scales.

The statistics of curvature,  $\kappa$ , and torsion,  $\tau$  of Lagrangian particle trajectories have been calculated for homogeneous and isotropic turbulence [15, 16, 17] and Rayleigh-Bénard convection [18]. Across all datasets, the same seemingly universal form for the probability density functions (PDFs) of curvature and torsion have been found, with low-curvature tails proportional to  $\kappa$  and high-curvature tails proportional to  $\kappa^{-2.5}$ , and low-torsion tails proportional to  $\tau^0$  and high-torsion tails proportional to  $\tau^{-3}$ . The power laws for governing both tails of the curvature PDFs and that describing high-torsion events can be derived assuming independent Gaussian statistics of velocity and acceleration [16, 18], which is not the case for turbulent flows. That is, curvature and torsion statistics are seemingly insensitive to details of the flow and in particular to at least low or moderate levels of anisotropy. The purpose of this paper is to compare curvature and torsion statistics across different flow configurations, including for the first time a turbulent boundary layer, and to introduce a more refined observable to quantify anisotropy in a geometric sense. As a first step towards a quantification of large-scale coherent motion on the geometry of tracer particle trajectories, we consider the entire flow to establish baseline statistics, focusing mainly on intrinsic anisotropy due to the presence of a mean flow.

We find that curvature and torsion PDFs for Rayleigh-Bénard convection (RBC) and von Kármán datasets can be mapped to a master curve after appropriate re-scaling with respect to the Taylor-scale Reynolds number. This may have been anticipated for the curvature since the bulk curvature statistics in RBC are the same as in homogeneous isotropic turbulence [18]. Here, we extend these results to torsion statistics. This assessment is corroborated by

the results for the zero-pressure-gradient (ZPG) boundary layer in the logarithmic region, where the torsion statistics agree with those of the aforementioned datasets. For curvature, the strong unidirectional flow in the ZPG turbulent boundary layer suppresses high curvature events, and low-curvature events become more likely compared to RBC and von Kármán flow. In contrast, the statistics of the curvature vector prove sensitive to even low levels of anisotropy. As such, we demonstrate the curvature vector to be a useful observable to provide a quantification of anisotropy in the Lagrangian frame of reference.

The paper is organised as follows. Section 2 outlines the required background in the differential geometry of space curves in the context of Lagrangian particle trajectories. The experiments, collected datasets and analysis methods are described in section 3. Section 4 contains a summary and comparison of velocity, acceleration, curvature and torsion statistics for the different datasets considered here. Our main results are presented in sec. 5, which focuses on the statistics of the curvature vector. We conclude with a summary of our results and provide suggestions for further research in section 6.

## 2. Curvature and torsion of space curves

We consider a Lagrangian particle trajectory  $\mathbf{x}(t)$  in a flow geometrically as given by the motion of a particle along a differentiable curve embedded in three-dimensional space. The Frenet-Serret formulae describe such curves through the respective rates of changes of the tangent vector  $\mathbf{t}$  to the curve, the vector normal to it,  $\mathbf{n}$  and the binormal vector  $\mathbf{b} = \mathbf{t} \times \mathbf{n}$  with respect to the arclength  $s$  of the curve

$$\frac{d}{ds}\mathbf{t} = \kappa\mathbf{n} , \quad (1)$$

$$\frac{d}{ds}\mathbf{n} = -\kappa\mathbf{t} + \tau\mathbf{b} , \quad (2)$$

$$\frac{d}{ds}\mathbf{b} = -\tau\mathbf{n} , \quad (3)$$

where  $\kappa = |d/ds \mathbf{t}|$  is the curvature and  $\tau = |d/ds \mathbf{b}|$  the torsion. Since  $\mathbf{t}$  is the tangent vector to the curve with respect to arclength, its rate of change will always be perpendicular to it, hence  $\mathbf{n}$  is normal to  $\mathbf{t}$ . For Lagrangian trajectories it is useful to express curvature and torsion as time derivatives of the particle position, that is velocity and acceleration, instead of in terms of the arclength of the curve

$$\kappa = \frac{|\mathbf{u} \times \mathbf{a}|}{|\mathbf{u}|^3} = \frac{|\mathbf{a}_n|}{|\mathbf{u}|^2} , \quad (4)$$

$$\tau = \frac{\mathbf{u} \cdot (\mathbf{a} \times \dot{\mathbf{a}})}{(\mathbf{u} \cdot \mathbf{u})^3 \kappa^2} , \quad (5)$$

where  $\mathbf{u}$  is the instantaneous velocity,  $\mathbf{a}$  the instantaneous acceleration and  $\mathbf{a}_n$  the acceleration component normal to the velocity vector, and  $\dot{\mathbf{a}}$  denotes the total time derivative of the acceleration.

As most flows in nature or engineering applications are not statistically homogeneous and isotropic, a measurement that reveals these broken statistical symmetries is needed. Curvature and torsion are global properties that measure the total instantaneous change in the shape of a trajectory. By construction, no information about the contributions to the total curvature stemming from the rate of change of the tangent vector to the curve in each coordinate direction is retained. In order to obtain such information, in what follows we define the *curvature vector*, and propose to consider the statistics of its projections onto coordinate directions defined by the experimental configurations.

### 2.1. Curvature vector

As introduced above, the curvature is defined as the magnitude of the rate of change of the tangent vector with respect to the arclength of the curve. In the context of anisotropy and a fixed coordinate system determined by the experimental apparatus, one may consider the rates of change of the tangent vector to a Lagrangian trajectory in the respective coordinate direction, expressed in terms of time derivatives

$$\frac{d}{ds}\mathbf{t} = \dot{\mathbf{t}} \frac{dt}{ds} = \frac{1}{|\mathbf{u}|} \dot{\mathbf{t}} . \quad (6)$$

Inspired by the definition of the signed curvature for planar curves and since the arclength derivative of the tangent vector is always perpendicular to the tangent vector, we define the curvature vector as the cross product between  $\mathbf{t}$  and  $d/ds \mathbf{t}$

$$\boldsymbol{\kappa} = \mathbf{t} \times \frac{d}{ds}\mathbf{t} = \mathbf{t} \times \frac{1}{|\mathbf{u}|} \dot{\mathbf{t}} = \frac{\mathbf{u} \times \mathbf{a}}{|\mathbf{u}|^3} , \quad (7)$$

and its absolute value is given by the expression for the curvature in eq. (4). The curvature vector, visualised in fig. 1 for an example trajectory, is perpendicular to the velocity  $\mathbf{u}$  and the acceleration vector  $\mathbf{a}$ , and is closely related to the bi-normal vector as part of the Frenet-Serret formulae. For planar curves, where  $\boldsymbol{\kappa}$  is always perpendicular to the plane the curve lies in, it corresponds to the signed curvature. To probe the effect of large-scale coherent flow structures and more generally anisotropy on the geometry of Lagrangian particle trajectories, we will discuss the statistics of the projection of this vector onto the  $x$ -,  $y$ - and  $z$ -directions, respectively,

$$\begin{aligned} \kappa_x &= \frac{1}{|\mathbf{u}|^3} u_y a_z - u_z a_y , \\ \kappa_y &= \frac{1}{|\mathbf{u}|^3} u_z a_x - u_x a_z , \\ \kappa_z &= \frac{1}{|\mathbf{u}|^3} u_x a_y - u_y a_x . \end{aligned} \quad (8)$$

The curvature vector quantifies what physical intuition would tell us about the geometry of particle trajectories in configurations with a strong mean flow. For instance, by eq. (8) a strong unidirectional flow should lead to smaller changes in

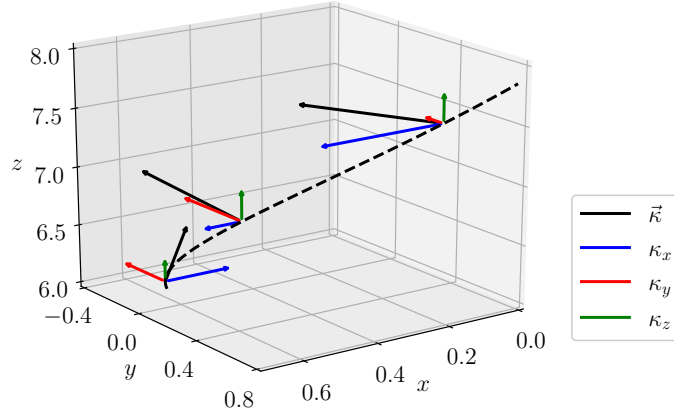


Figure 1: Curvature vector of a trajectory and projections onto the  $x$ -,  $y$ - and  $z$ - directions. The dashed line represents a space curve, the colors indicate the different directions, and curvature vector, as defined in eq. (8), is shown in black.

the tangent vector to the curve in the mean flow direction and hence one may expect a higher probability of small values of the curvature in this direction compared to the other coordinate directions. We will see in sec. 5 that this is indeed the case.

Finally, considering again the expressions for the components of the curvature vector given in eq. (8), we note that the same argument that determines the shape of the right tail of the curvature PDF [16] may be applied here to the PDFs of the curvature vector components. In contrast, for the left tail no such correspondence applies.

### 3. Methods and Data

The analysed data consists of a turbulent von Kármán flow, Rayleigh-Bénard convection at two different Rayleigh numbers and a ZPG turbulent boundary layer. Key properties and observables of the experiments are provided in table 1, and descriptions of the different experimental configurations and obtained datasets are provided below. For all datasets, a global coordinate system is used, that is the standard Rayleigh-Bénard convection setup where  $x$ - and  $y$ -directions define the horizontal plane and  $z$  is the vertical direction normal to the heated bottom plate. Therefore the coordinate system for the boundary layer here has its wall-normal direction in  $z$ -direction rather than the commonly used  $y$ -direction. In all cases, the experimental error is estimated as noise using a spectral analysis of the particle positions. The amplitude spectrum falls off with a specific slope, until it turns towards a constant value for high frequencies. The

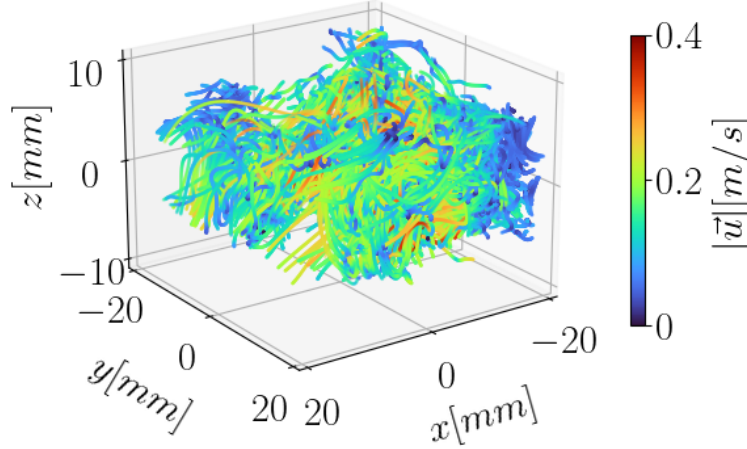


Figure 2: Visualisation of a subset of tracer particle trajectories in von Kármán flow. The colour bar indicates the absolute value of the velocity.

positional error  $\Delta x$  of the raw particle tracks can be estimated as the height of this constant level [19].

All data is processed using the Shake-The-Box (STB) algorithm [20, 21] which is described in the following. STB is used for the three-dimensional investigation of flows by tracking tracer particles even in conditions of high particle image density. A system of multiple cameras records time-resolved images of the tracer particles, being illuminated by a suitable light source (typically a high-speed laser or LEDs). STB employs Iterative Particle Reconstruction [22, 23] to reconstruct 3D particle positions, combined with a temporal predictor-corrector scheme of known tracks. The combination of these methods allows to track particles in high numbers, while avoiding the generation of false (ghost) tracks.

### 3.1. von Kármán flow

The experiment was carried out by DLR Göttingen at the von Kármán facility at the MPI Göttingen [24]. The device consists of two counter-rotating propellers of 500 mm diameter in a tank filled with water rotating with frequency  $f_p = 0.5 \text{ Hz}$ . That generates approximately homogeneous and isotropic turbulence in a small volume in the center of the flow chamber where the coordinate system is chosen in a way that the propellers are located in  $z$ -direction. The flow is seeded with Dynoseeds TS20 as tracer particles which have a diameter of  $20 \mu\text{m}$  and are illuminated by a high-repetition speed laser. The camera system recording the flow consists of four cameras operating at  $1250 \text{ Hz}$ , leading

	vK	RBC I	RBC II	BL
$Re_\lambda$	270	146	183	30
$Re_\tau$	—	—	—	2295
$\tau_\eta[s]$	0.013	0.35	0.18	$0.08 \cdot 10^{-3}$
$f[Hz]$	1250	20	30	1000
$\tau_\eta \cdot f$	16.25	7	5.4	0.09
$\eta[mm]$	0.1	2.3	1.7	0.037
$\Delta x[\mu m]$	3	50	50	30
$\eta/\Delta x$	33	96	70	1.2
$\ell[\mu m]$	20	300	220	300
$\eta/\ell$	5	0.77	0.77	0.12
$f_p[Hz]$	0.5	—	—	—
$\bar{U}[m/s]$	—	—	—	(7, 0, 0)
$Ra[10^8]$	—	$5.25 \pm 0.06$	$15.3 \pm 0.3$	—
$Pr$	—	0.7	0.7	—
$\Delta T[K]$	—	$4.03 \pm 0.06$	$11.8 \pm 0.2$	—
$\Gamma$	—	1	1	—
$\lambda_b[mm]$	—	11.5	8.5	—
$V[cm^3]$	$0.4 \times 0.4 \times 0.15$	$55^2\pi \times 110$	$\pi 55^2 \times 110$	$280 \times 80 \times 25$
$V_m[cm^3]$	$0.4 \times 0.4 \times 0.15$	$52.5^2\pi \times 104.5$	$52.5^2\pi \times 104.5$	$100 \times 80 \times 3.5$
$N$	92739514	1287242	12150782	99286611

Table 1: Parameters and key observables of the analysed datasets, von Kármán flow (vK), Rayleigh-Bénard convection (RBC) and the ZPG turbulent boundary layer (BL). The Taylor-scale Reynolds number is  $Re_\lambda = \sqrt{15}(U_{\text{rms}})^2\eta^2/\nu^2$  where  $U_{\text{rms}} = \sqrt{1/3 (\langle u_x^2 \rangle + \langle u_y^2 \rangle + \langle u_z^2 \rangle)}$  is the root-mean-square of the velocity fluctuations in the different directions,  $\eta$  the Kolmogorov length-scale,  $\tau_\eta$  the Kolmogorov time-scale, and  $\nu$  viscosity. The friction Reynolds number is  $Re_\tau = \frac{u_\tau \delta}{\nu}$ , with  $u_\tau = \sqrt{\tau_W/\rho}$  where  $\tau_W$  is the wall-shear stress,  $\delta$  the boundary-layer thickness and  $\rho$  the density;  $f$  is the camera (sampling) frequency and  $\Delta x$  the experimental uncertainty measured spectrally [19]. The spatial uncertainty based on the requirement of smooth correlation functions with expected zero-crossings is  $\ell$ , a more detailed explanation of this parameter can be found in sec. 3. Flow-specific properties and parameters are the propeller frequency  $f_p$  for von Kármán flow and the mean velocity  $\bar{U}$  for the boundary layer. For the RBC, we have the Rayleigh number  $Ra = g\alpha\Delta TH^3/(\nu\kappa)$ , Prandtl number  $Pr = \nu/\kappa$ , with  $g$  the gravitational acceleration,  $\alpha$  the isobaric expansion coefficient,  $\kappa$  the thermal diffusivity,  $H$  the cell height and  $\Delta T$  the temperature difference between top and bottom plate. The aspect ratio is denoted by  $\Gamma$  and the thickness of the thermal boundary layer by  $\lambda_b = H/(2Nu)$ , with  $Nu$  the Nusselt number. The volume  $V$  is the volume where the trajectories are recorded,  $V_m$  the sub-volume considered for our calculations, and  $N$  is the number of total number of trajectories, histograms of trajectories lengths are shown in fig. 5.

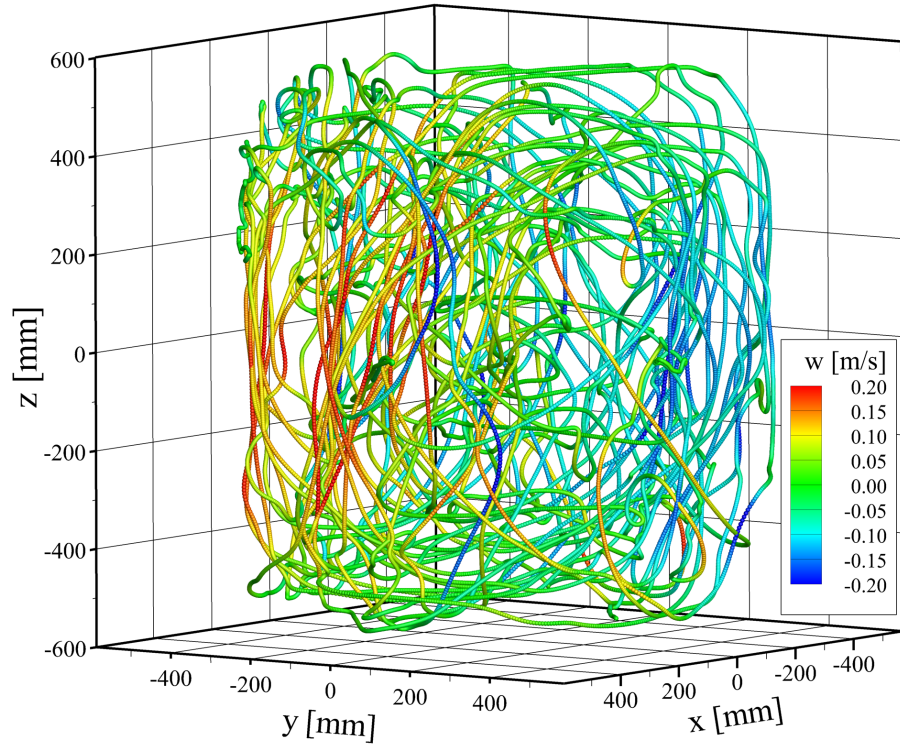


Figure 3: Visualisation of a single long tracer particle trajectory in Rayleigh-Bénard convection at  $Ra = 1.53 \cdot 10^9$ . The colour bar indicates the vertical component of the velocity.



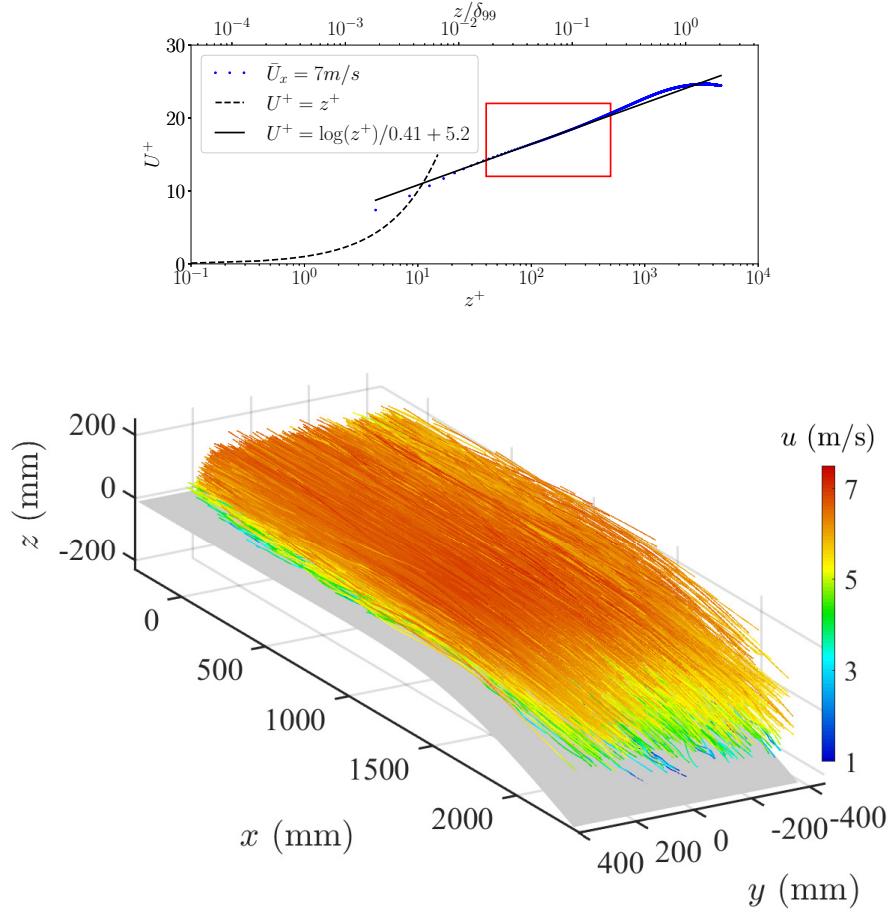


Figure 4: Turbulent boundary layer. Top: Stream-wise mean velocity as a function of the distance to the wall, measured in  $+$ -units where  $U^+ = u_x/u_\tau$  and  $z^+ = z u_\tau/\nu$  with  $u_\tau$  the friction velocity and expected velocity profiles. The data clearly follows the logarithmic law from around  $z^+ = 30$  to  $z^+ = 500$ . The box indicates the volume used for the analysis presented here. Bottom: Visualisation of a subset of tracer particle trajectories within a turbulent boundary layer colored with stream-wise velocity. The ZPG region analysed here extends from  $x = 0\text{mm}$  until  $x = 1000\text{mm}$ .

to a high temporal resolution ( $\tau_\eta \cdot f = 16.25$ ), where  $\tau_\eta$  is the Kolmogorov time scale. To track the tracer particles the Shake-The-Box algorithm is applied, yielding up to 100000 tracked particles per time step in a volume of approximately  $40 \times 40 \times 15 \text{ mm}^3$ . A visualisation of a subset of particle trajectories provided in fig. 2.

### 3.2. Rayleigh-Bénard convection

Both datasets of the Rayleigh-Bénard convection were generated at the DLR Göttingen [25]. The Rayleigh numbers are  $Ra = 5.25 \cdot 10^8$  (RBC I) and  $Ra = 1.53 \cdot 10^9$  (RBC II) for the two different datasets. The experimental set up contains a cylindrical convection cell filled with air at aspect ratio  $\Gamma = 1$  and height  $H = 1.1 \text{ m}$  in  $z$ -direction and the top and bottom plate in the  $xy$ -plane. To ensure constant heating at the bottom, the plate is an electrically heated aluminium plate and for constant cooling at the top, the top plate is water perfused. The flow is seeded with helium filled soap bubbles as tracers with a diameter of  $370 \mu\text{m}$  with an average life expectancy of  $326 \text{ s}$ . The flow is illuminated by 849 pulsed LEDs placed above the top plate and synchronised with a system of six scientific cameras operating at  $20 \text{ Hz}$  and  $30 \text{ Hz}$  for the two different cases. The tracking of over 500000 tracer particles is again carried out using the Shake-The-Box algorithm. A visualisation of single long trajectory is provided in fig. 3. Further details of the experiment and flow visualisations including a video introduction to the experiment are provided in Refs. [25, 26]. We point out that large-scale motion in form of the large-scale circulation (LSC) is observed in both datasets, see Ref. [26].

### 3.3. Turbulent boundary layer

The last dataset considered is of a turbulent boundary layer with ZPG [27] and a bulk flow velocity of  $7 \text{ m/s}$ . The experiment was conducted in the atmospheric wind tunnel at the Universität der Bundeswehr München as part of a joint campaign between the University and the DLR. The wind tunnel has a  $22 \text{ m}$  long test section with a  $7 \text{ m}$  long boundary layer model installed on the side wall several meter downstream from the beginning of the test section. The boundary layer model consists of an S-shaped flow deflection and a downstream straight ramp designed to produce strong adverse pressure gradients up to separation. In between the flow deflections, a  $4 \text{ m}$  long flat plate is installed over which ZPG conditions are present. The analysis carried out here is restricted to the logarithmic layer ( $z^+ = 40 - 500$ ) of the turbulent boundary layer in the ZPG region, as indicated by the box in fig. 4(top).

The camera system consists of twelve high speed cameras operating at  $1000 \text{ Hz}$  recording a volume of approximately  $2800 \times 800 \times 250 \text{ mm}^3$  in stream-wise  $\times$  span-wise  $\times$  wall-normal direction. The ZPG region was fully recorded with a length of  $1800 \text{ mm}$  in stream-wise direction. Ten high power LED arrays, installed above the wind tunnel, illuminated the flow containing helium filled soap bubbles as tracers. Up to 600000 bubbles can be tracked instantaneously within the full volume over time-series of approximately 1382 images using the

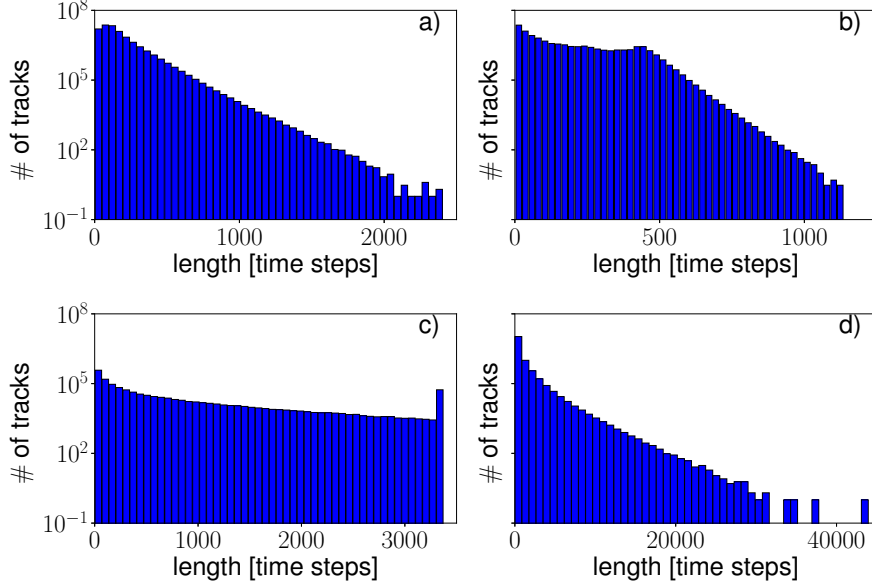


Figure 5: Histograms of trajectory length for a) von Kármán flow, b) boundary layer, c) RBC I and d) RBC II. The histograms are of the full measurement volume  $V$ . Trajectories considered for the analysis have a minimal length of 100 time steps.

DLR Shake-The-Box implementation. A visualisation of a subset of particle trajectories provided in fig. 4 (bottom). A more detailed explanation of the experimental set up, calibration and the Lagrangian particle tracking can be found in Ref. [27]. We point out that turbulent superstructures in form of coherent structures of considerable stream-wise extent are observed in this dataset, see Ref. [27], fig. 5.

### 3.4. Data processing

As curvature and torsion involve derivatives up to order three, we need to calculate these as part of our analysis. We fit B-Splines of order five to the particle positions and calculate the derivatives of these. We only use trajectories consisting of at least 100 time steps. Histograms of the trajectory lengths are presented in fig. 5. To fit B-Splines a smoothness parameter  $\ell$ , essentially a filter scale to account for experimental uncertainty, is required and needs to be chosen appropriately. Its value is related to a spatial measurement uncertainty where  $\Delta x = \ell$ . In all experiments, the uncertainty on of particle positions has been determined by the spectral method described above [19]. For the analysis we will determine the spatial uncertainty through  $\ell$  rather than using the experimental accuracy as determined by the spectral method, because the former turns out to be always larger than the latter, as we will see in what follows. To estimate

the  $\ell$ -value, we use the acceleration auto-correlation functions for calibration

$$R_i(\tau) = \langle a_i(t) \cdot a_i(t + \tau) \rangle, \quad (9)$$

where  $a_i(t)$  is the instantaneous acceleration in the  $i^{th}$ -direction. The auto-correlation functions are only calculated for trajectories that lie fully in a selected sub-volume,  $V_m$ , which for Rayleigh-Bénard convection excludes thermal an side-wall viscous boundary layers and for the turbulent boundary layer restricts our calculations to the logarithmic region, see table 1) for further details. To decide on the appropriate value for the smoothness parameter, we have different constraints depending on the different datasets. We require in all cases that the autocorrelation function is smooth without any nonphysical oscillations and has a first zero-crossing where expected from previous analyses. For the von Kármán data, a zero-crossing around  $2.2 \tau_\eta$  is expected [28, 29], and similarly for Rayleigh-Bénard convection [30]. Stelzenmuller *et al.* [31] calculated the auto-correlation function in turbulent channel flow, based on the initial height of the particles. For span-wise and wall normal direction, the zero-crossing of the auto-correlation function is also found to be around  $2\tau_\eta$  and shifted to a higher value in stream-wise direction. We expect the same behaviour for the boundary layer dataset, as the analysed heights in both cases are where the mean velocity follows the logarithmic law, see also fig. 4 (top).

For the von Kármán flow a smoothness parameter of  $\ell = 0.02 \text{ mm}$  is needed to obtain the expected zero-crossing (fig. 6 a)). This refers to a spatial uncertainty of  $20 \mu\text{m}$  which is about one order of magnitude higher than the experimental accuracy of  $3 \mu\text{m}$  determined spectrally [19]. For the two datasets of a Rayleigh-Bénard convection, a smoothness parameter of  $\ell = 0.3 \text{ mm}$  and  $\ell = 0.22 \text{ mm}$  for the  $Ra = 5.25 \cdot 10^8$  and  $Ra = 1.53 \cdot 10^9$  case respectively (fig. 6 c), d)) is used. For both datasets the experimental accuracy is estimated to be  $50 \mu\text{m}$ , therefore the spatial uncertainty estimated here is again about one order of magnitude higher than that determined by the spectral method [19]. For the boundary layer, a smooth correlation function is obtained using  $\ell = 0.3 \text{ mm}$  (fig. 6 b)) which also agrees with the previous datasets that the  $\ell$ -value is around ten times larger than the experimental uncertainty obtained from the spectral method [19]. However, the zero-crossing of the correlation function in this case is around  $180 \tau_\eta$  and is approximately of the same order for all the different directions. The stream-wise direction has its zero-crossing around  $220 \tau_\eta$ , thus is shifted to higher values for the stream-wise direction. As one time step is  $\approx 11 \tau_\eta$  and therefore much larger than the expected correlation of  $2 \tau_\eta$ , we assume this to be the cause of the long correlations. We therefore will mainly focus on the comparison between the von Kármán flow and Rayleigh-Bénard convection, and discuss the ZPG boundary layer mentioning caveats on resolution where necessary.

#### 4. Velocity, acceleration, curvature and torsion

The following sections present probability density functions (PDFs) of velocity, acceleration, curvature and torsion for the previously described datasets.

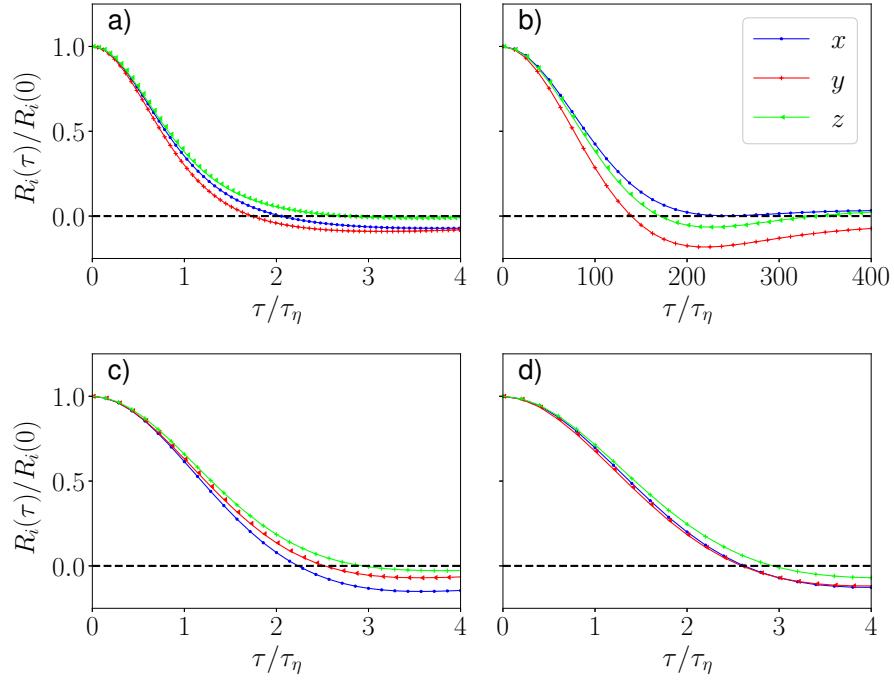


Figure 6: Normalised auto-correlation functions a) for von Kármán-flow with zero-crossing around  $2 \tau_\eta$  as expected from analysis in [28, 29] using a smoothness value of  $\ell = 0.02 \text{ mm}$ . b) For BL using  $\ell = 0.3 \text{ mm}$  with zero-crossing around  $180 \tau_\eta$ , discussion in text. In c) and d) auto-correlation of RBC with  $Ra = 5.25 \cdot 10^8$  and  $Ra = 1.53 \cdot 10^9$  respectively, both cases show a zero-crossing around  $2.2 \tau_\eta$  as found in [30]. Smoothness values used in these cases are c)  $\ell = 0.3 \text{ mm}$  and d)  $\ell = 0.22 \text{ mm}$ .

We compare the results with literature as well as between the different datasets, focusing in the first instance on similarities and differences between the respective curves and model predictions assuming statistical homogeneity and isotropy [16], and subsequently also on the effect of the Taylor-scale Reynolds number  $Re_\lambda$ .

#### 4.1. von Kármán flow

Figure 7 a) presents the standardised PDFs of each velocity component of the von Kármán flow at  $Re_\lambda = 270$ , with PDFs of  $u_x$  and  $u_z$  being approximately Gaussian as expected and first reported in Refs. [32, 33]. The PDF of  $u_y$ , however, has super-Gaussian tails, indicating that extreme velocity fluctuations are more likely in the  $y$ -direction compared with the  $x$ - and  $z$ -directions. That is, large-scale fluctuations occur that break statistical isotropy, it is known indeed that von Kármán flow is not fully isotropic [34]. Its large-scale dynamics is dominated by a shearing and a pumping mode, the former being the result of the counter-rotating propellers, while the latter drives fluid first inwards and subsequently upwards towards the propellers through centrifugal pumping, see the visualisations in fig. 11 of ref. [35]. Furthermore, as the ratio of transverse and axial components of the rms velocity varies only weakly with propeller speed about a value of 1.5, the large-scale dynamics appears not [35]. Statistical isotropy is restored at small scales as can be seen by inspection of and comparison between the standardised PDFs of each acceleration component shown in fig. 7 b). All PDFs have similarly wide tails, in qualitative agreement with known results on Lagrangian acceleration statistics in homogeneous and isotropic turbulence obtained from numerical data [36, 37, 38, 28, 39] and experimental data [40, 41, 38, 39]. For a quantitative comparison, we consider numerical data at a slightly higher value of  $Re_\lambda = 350$  and slightly lower resolution  $\eta/\Delta x = 3$  [36], where extreme events up to 40 times the standard deviation occur with probabilities around  $10^{-7}$ , see figure 3(a) of Ref. [36]. As can be seen from fig. 7 b), our results are commensurate with these values.

Curvature and torsion PDFs are shown in figs. 8 a) and b), respectively, and we observe the expected power laws for left and right tails of the PDFs as in previous work on curvature and torsion statistics in homogeneous and isotropic turbulence using either DNS data for curvature and torsion [15, 17] or experimental data for curvature only [16]. That is, the left tail of the curvature PDF that corresponds to small-curvature events is proportional to  $\kappa\eta$  while the right tail that corresponds to high-curvature events scales as  $(\kappa\eta)^{-2.5}$ . For the torsion PDF we find  $P(\tau) \sim (\tau\eta)^0$  for low-torsion events and  $P(\tau) \sim (\tau\eta)^{-3}$  for high-torsion events. These curvature PDF exponents can be derived assuming independent Gaussian statistics for velocity and acceleration [16], similar arguments apply to the exponent describing the right tail of the torsion PDF [17, 18]. Acceleration statistics in developed turbulence are not Gaussian and velocity and acceleration statistics are not independent either [28]; however, using a recently developed decomposition technique of Lagrangian statistics into Gaussian sub-ensembles [36], the PDF exponents can be derived without these assumptions [42].

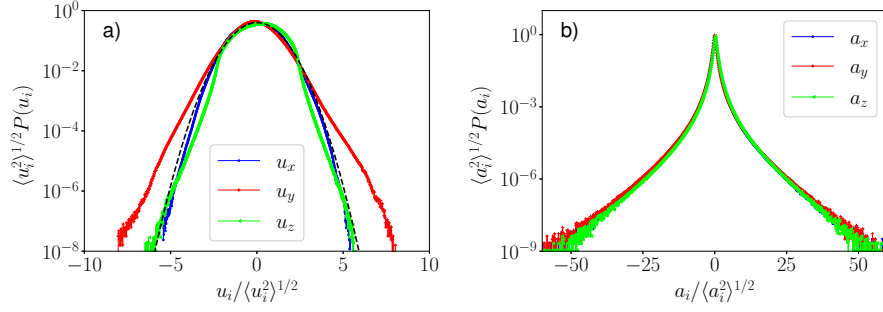


Figure 7: Standardised PDFs of a) velocity, b) and acceleration components for von Kármán flow on semi-logarithmic scales. The dashed line in a) corresponds to a Gaussian with zero mean and a standard deviation of unity.

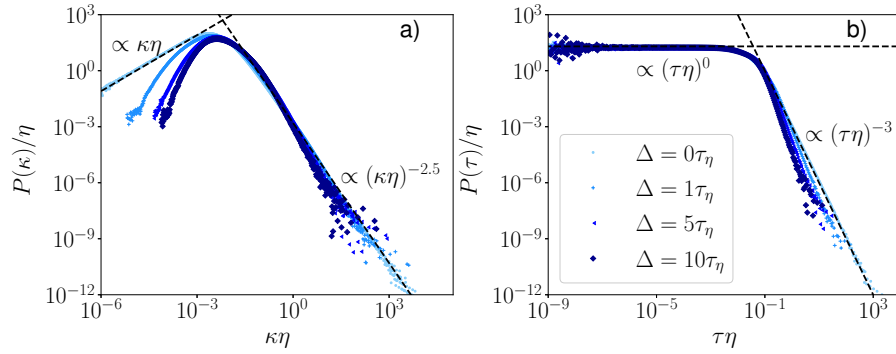


Figure 8: a) Curvature PDFs and b) torsion PDFs for the von Kármán dataset. PDFs of averaged curvature and torsion over different time windows  $\Delta$ , light blue no averaging, dark blue  $\Delta = 10 \tau_\eta$ .

Rather than connecting curvature with vortical flow structures, Xu *et al.* [16] showed that large-scale flow reversals affect curvature statistics and suggest to filter out these events in order to probe the more intuitive idea that connects curvature with vorticity. As large-scale flow reversals generally occur on short time scales, the filtering was implemented by averaging the curvature along a trajectory over a small interval in time. Such filtering is also useful to detect correlations between high-normal-acceleration events and vortex filaments [43].

To compare with previous measurements of curvature statistics and extend to torsion statistics, we filtered curvature and torsion along each trajectory for time intervals of one, five and ten Kolmogorov times with results shown in figs. 8 a) and b) alongside the unfiltered case for curvature and torsion, respectively. For the curvature PDFs of the filtered data, the right tail corresponding to large values of the curvature seems to remain relatively stable, while we observe significant differences between the left tails of the PDFs associated with small values of the curvature compared with the unfiltered case. Small values of curvature are becoming increasingly less likely with increasing filter scale. Similar results have been reported by Xu *et al.* [16], albeit with more profound effects in the high-curvature tail. For torsion PDFs, we observe the opposite trend, with the low-torsion tail remaining largely unaffected by the filtering while high torsion events become less likely with increasing filter width. Disregarding potential correlations, such behaviour can be explained by inspection of eq. (5) that describes the torsion, where the curvature appears in the denominator. Hence a suppression of low curvature events can plausibly result in a suppression of high torsion events.

#### 4.2. Rayleigh-Bénard Convection

In what follows we consider velocity, acceleration, curvature and torsion statistics for the two RBC datasets described in section 3 with Rayleigh numbers  $Ra = 5.25 \cdot 10^8$  and  $Ra = 1.53 \cdot 10^9$ , respectively. We focus on the bulk by conditioning the statistics on wall-distance in both vertical and horizontal directions resulting in the measurement domains  $V_m$  reported in table 1. In the vertical as well as horizontal directions we disregard data at distances of less than  $2.4 \lambda_b$  for RBC I and  $3.2 \lambda_b$  for RBC II from the different walls.

Velocity and acceleration statistics for both datasets are presented in fig. 9. Figures 9 a), b) present velocity-component PDFs for RBC I and RBC II, respectively. From subfigure a) it can be seen that for the lower- $Ra$  case the PDF of  $u_x$  is approximately Gaussian while those of the remaining directions have sub-Gaussian tails. For the higher- $Ra$  case, the velocity PDFs in subfigure b) are approximately Gaussian for both horizontal directions while only the velocity PDF in the vertical  $z$ -direction is slightly sub-Gaussian. The more pronounced sub-Gaussianity in the lower- $Ra$  case compared to the higher- $Ra$  case may be connected to a less perturbed large-scale circulation in the former case. Interestingly, the deviations from Gaussianity in both cases are smaller than for the von Kármán flow.

Acceleration PDFs for RBC I and RBC II are shown in 9 c), d), respectively. As can be seen by comparison of the data in the two subfigures, the PDFs in  $x$ -



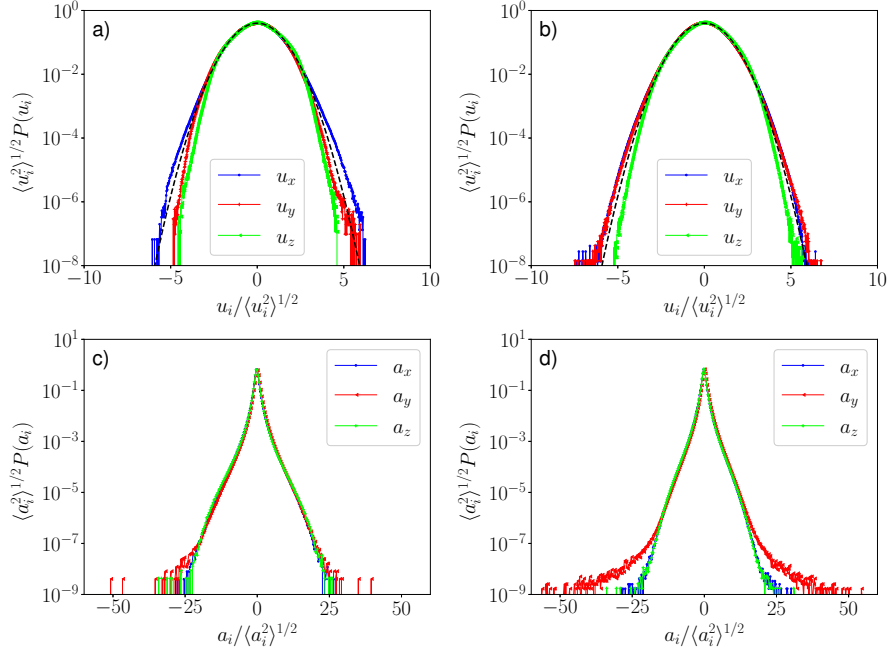


Figure 9: Standardised velocity and acceleration PDFs for Rayleigh-Bénard convection. Top row: velocity components for a)  $Ra = 5.3 \cdot 10^8$  and b)  $Ra = 1.53 \cdot 10^9$ . The black dashed line corresponds to a Gaussian with zero mean and unit variance. Bottom row: acceleration components for c)  $Ra = 5.3 \cdot 10^8$  and d)  $Ra = 1.53 \cdot 10^9$ .

and  $z$ -directions are very similar in shape with fluctuations up to 25-30 times the root-mean-square value. In contrast, extreme acceleration events in  $y$ -direction are much more likely for the higher- $Ra$  case and root-mean-square values up to 55 occur, similar to the von Kármán case. As  $Re_\lambda = 270$  is much higher for the von Kármán data, than for the two RBC datasets which corresponds to  $Re_\lambda \approx 146$  and  $Re_\lambda \approx 183$ , one could have expected wider tails for the von Kármán acceleration PDFs compared to the RBC datasets. Interestingly, the small scales in RBC become more anisotropic with increasing  $Ra$ , with the  $y$ -direction being more intermittent – its acceleration PDFs change with Reynolds number – than the remaining two directions. The measurements presented here for  $Ra = 5.3 \times 10^8$  commensurate with those reported by Schumacher [44] in the bulk for numerical simulations at  $Ra = 1.2 \times 10^8$  in a domain with free-slip boundary conditions on the top and bottom plate and periodic boundary conditions in the transverse directions. The reason for the asymmetry between the two transverse directions in the higher- $Ra$  case is not clear.

Figure 10 presents filtered and unfiltered curvature and torsion PDFs for both datasets. For both observables and both Rayleigh numbers, we find the same power laws as in the case for homogeneous and isotropic turbulence, turbu-

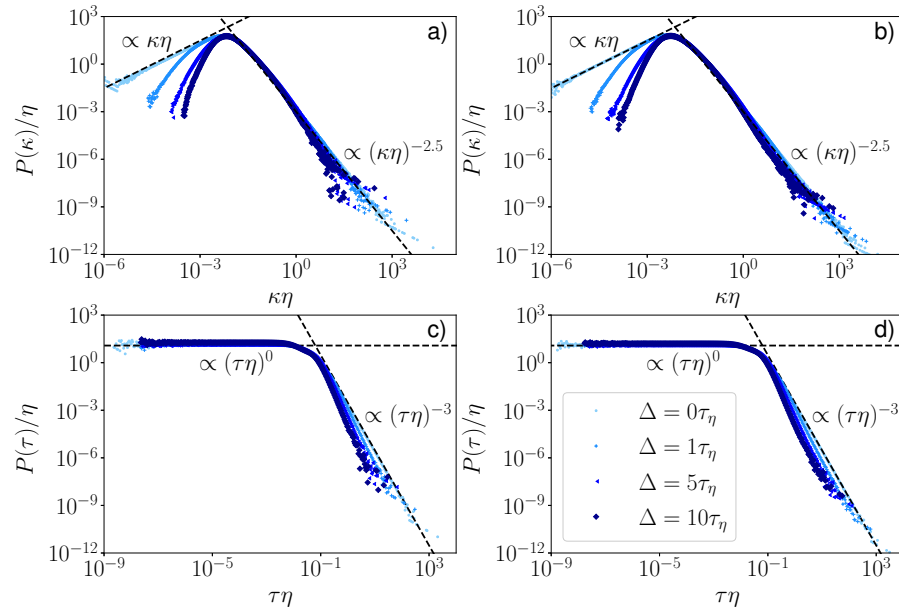


Figure 10: Filtered and unfiltered curvature and torsion statistics for Rayleigh-Bénard convection, where  $\Delta$  is the filter width. Top row: curvature PDFs for a)  $Ra = 5.3 \cdot 10^8$  and b)  $Ra = 1.53 \cdot 10^9$ . Bottom row: torsion PDFs for c)  $Ra = 5.3 \cdot 10^8$  and d)  $Ra = 1.53 \cdot 10^9$ .

lent von Kármán flow and previous works on non-rotating and rotating Rayleigh-Bénard convection and rotating electromagnetically forced turbulence [18]. For the unfiltered case, the PDF of the non-dimensionalised curvature is linear for small values and proportional to  $(\kappa\eta)^{-2/5}$ , for the torsion the PDF is constant for small values and the right tail follows a power law with exponent of -3. Filtering out flow reversals by averaging curvature and torsion along each trajectory leads to a similar behaviour than for the von Kármán flow where the tail for high values of the curvature does not change while for small values of the curvature, the power law changes and *vice versa* for the torsion.

#### 4.3. Turbulent boundary layer

For the ZPG boundary layer we focus only on the logarithmic region, that is, distances of  $z^+ = 40 - 500$  from the bottom wall. This dataset differs substantially from the von Kármán and RBC datasets. Firstly, the boundary layer is a driven flow with a strong mean velocity in  $x$ -direction, see table 1. Second, the temporal resolution is much lower, with images taken about each  $10 \tau_\eta$ , see table 1. That is, small-scale dynamics are not sufficiently well resolved in the measurements which results in an effective filtering when fitting the B-splines, and we cannot draw firm conclusions on small-scale statistics. Therefore we focus mainly on the effect of the mean flow. In what follows we discuss resolution effects where appropriate.

PDFs of velocity and acceleration components in stream-wise, span-wise and wall-normal directions are shown in fig. 11 a), b), respectively. As can be seen from in subfigure a), the PDF of the stream-wise velocity component  $u_x$  has nonzero mean and clearly sub-Gaussian tails. The PDFs of the velocity in span-wise  $y$ -direction and wall-normal  $z$ -direction both have sub-Gaussian tails but approximately zero mean. These clear indications of anisotropy are not present in the PDFs of stream-wise, span-wise and wall-normal acceleration components, which fluctuate very similarly as can be seen from the data shown in subfigure b). However, the boundary layer dataset has less extreme acceleration events, the most likely explanation for this is the temporal resolution of  $\tau_\eta \cdot f = 0.09$ , where  $f$  is the camera frequency, such that extreme events cannot be resolved. We tested this hypothesis with the RBC II dataset only using every 68th data snapshot to match the temporal resolution of the boundary layer data, and found the tails of the resulting acceleration PDFs to be similarly suppressed (not shown). That is, we cannot rule out that the apparent return to isotropy at the small scales observed here is an artefact of low resolution, as potential differences in the tails of the PDFs cannot be resolved. For a further analysis of Eulerian and Lagrangian statistics obtained from the same dataset, see Ref. [45].

Having discussed velocity and acceleration statistics, we now focus on — to the best of our knowledge first — measurements of curvature and torsion fluctuations in the ZPG boundary layer. The most striking observation here is that the right tail of the curvature PDF differs significantly from the curvature PDFs of the previously discussed datasets and from those reported in Refs. [16, 15, 18]. The left tail of the curvature PDF is still linear, however, low curvature events are more likely in the turbulent boundary layer compared to the aforementioned

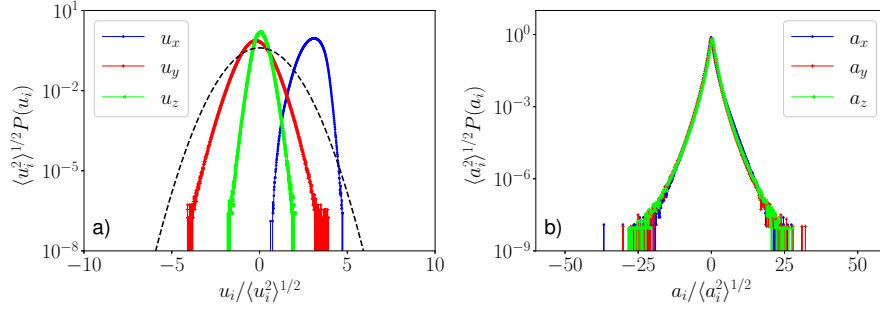


Figure 11: Standardised PDFs of velocity a) and acceleration b) components in the logarithmic region of a ZPG turbulent boundary layer over a flat plate using the root-mean-square (rms) of velocity fluctuations for the velocity and the rms of the acceleration for acceleration PDFs. The dashed line in a) corresponds to a Gaussian with zero mean and unit variance.

datasets. The right tail of the PDF does not have power law form, and is much lighter than for the for the aforementioned datasets. To explain this observation, we recall that the formula for the curvature is  $\kappa = a_n/u^2$ , and extreme curvature events are generated mainly by low-velocities events, rather than by high acceleration events [16]. A strong unidirectional flow results in low-velocity events to be less likely, resulting in less high curvature events. Importantly, we do not expect the temporal resolution to play a crucial role here as for the underresolved RBC test-dataset, we still obtained the same power laws for the curvature PDF as for the full data (not shown). While the right tail of the curvature PDF is strongly influenced by large-scale motions, the torsion PDF has power law tails with the same exponents as observed for the other datasets discussed here. Importantly, high torsion values are less likely and low-torsion events more likely to occur in the ZPG turbulent boundary layer as compared to von Kármán flow and RBC, which can be interpreted as trajectories in a flow with a strong stream-wise velocity component to be less twisted.

#### 4.4. Quantitative comparison of curvature and torsion statistics

Curvature and torsion have units of inverse length and can be made dimensionless by the ratio of the rms-value of the acceleration and the velocity variance [16], that is,

$$\kappa = \frac{|\mathbf{a}_n|}{|\mathbf{u}|^2} \propto \frac{\langle a^2 \rangle^{1/2}}{\langle u^2 \rangle}, \quad (10)$$

$$\tau = \frac{\mathbf{u} \cdot (\mathbf{a} \times \dot{\mathbf{a}})}{|\mathbf{u}|^3 \kappa^2} \propto \frac{\langle u^2 \rangle^{1/2} \langle a^2 \rangle^{1/2} \langle \dot{u}^2 \rangle^{1/2}}{\langle u^2 \rangle^{3/2} \left( \frac{\langle a^2 \rangle^{1/2}}{\langle u^2 \rangle} \right)^2} = \frac{\langle a^2 \rangle^{1/2}}{\langle u^2 \rangle}. \quad (11)$$

Based on Kolmogorov's original scaling arguments [46, 47], Heisenberg and Yaglom [48, 49] derived the following scaling relation for the acceleration covariance

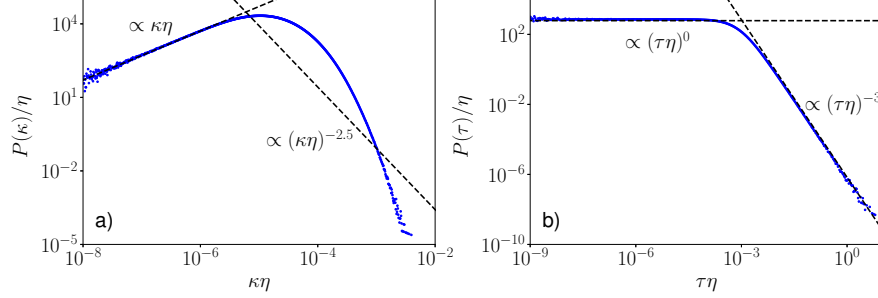


Figure 12: a) Curvature and b) torsion PDFs for the logarithmic layer in a ZPG turbulent boundary layer. Deviations of the expected power laws for the curvature are discussed in the text.

(cf. [40, 35])

$$\langle a_i a_j \rangle = a_0 \varepsilon^{3/2} \nu^{-1/2} \delta_{ij} , \quad (12)$$

where  $a_0$  does not depend on the Reynolds number for K41 scaling. In conjunction with eqs. (10) and (11), Heisenberg-Yaglom scaling results in a Reynolds-number-dependent non-dimensionalisation of curvature [16] and torsion and thus enables a comparison of PDFs for data at different Reynolds numbers. For von Kármán flow, curvature PDFs for  $200 \leq Re_\lambda \leq 815$  indeed collapse onto a master curve [16].

Here, we use the same ansatz to compare the PDFs of curvature and torsion for von Kármán flow and Rayleigh-Bénard convection at different Reynolds numbers with results shown in figs. 13 a), b). Curvature and torsion PDFs pertaining to the three different datasets collapse onto respective master curves. This confirms that in the bulk, the form of the curvature and torsion PDFs are only determined by velocity and acceleration fluctuations and do not depend on the geometry of the flow or the type of turbulence production, as suggested in Ref. [18], at least for RBC or, more generally, relatively low levels of anisotropy. As the curvature PDF for the turbulent boundary layer is phenomenologically different from the curvature PDFs of the von Kármán and RBC data, it is not included in the comparison. However, even the torsion PDF of the turbulent boundary layer could not be re-scaled with  $Re_\lambda$  using Heisenberg-Yaglom scaling to fit on the torsion master curve, which may be connected to the low value of Taylor-scale Reynolds number,  $Re_\lambda = 30$ .

## 5. Curvature vector statistics

As seen in previous sections, large-scale turbulent fluctuations in all presented datasets are statistically anisotropic, either due to the motion and location of the propellers in the von Kármán experiment, the direction of a temperature gradient and the ensuing presence of the LSC in Rayleigh-Bénard convection (i.e. the remnants of a superstructure) or a strong unidirectional flow and

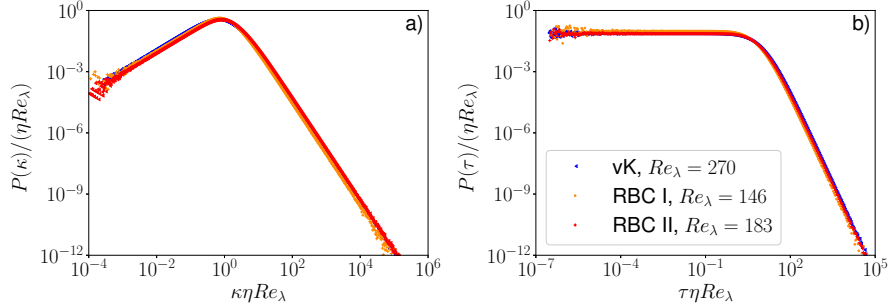


Figure 13: Heisenberg-Yaglom scaled PDFs of a) curvature and b) torsion for von Kármán flow and Rayleigh-Bénard convection, for the latter in the bulk only.

the presence of large-scale coherent structures in the ZPG turbulent boundary layer.

As discussed in section 4, curvature fluctuations are insensitive to anisotropy, unless the degree of anisotropy is appreciably large – a quantification thereof may be addressed in future work – and differences in curvature fluctuations between the respective datasets are only due to Reynolds number. This may not be too surprising, since curvature as a global observable is coordinate-independent and mixes information pertaining to the different spatial directions. As such, it can only provide information on how curved trajectories in general are in a flow. To provide further insight into how large-scale motion affects the geometry of particle trajectories, we now focus on the statistics of the curvature vector, which can give a measure of anisotropy of the flow as detailed in sec. 2.

Figure 14 shows the PDFs of the absolute value of the projection of the curvature vector onto the  $x$ -,  $y$ - and  $z$ -directions for the four different datasets. A few general observations can be made for all datasets. Firstly, the left tails of the PDFs are constant in all cases. The corresponding plateaux distinguish between the different directions, as can be seen from the insets in figs. 14 a), c), d) and directly in fig. 14 b). Second, the right tails, which describe high-curvature events in the respective spatial directions have the same power law as the curvature PDF for von Kármán flow and Rayleigh-Bénard convection, which may be expected as discussed in sec. 2. For the ZPG boundary layer, the high-curvature tails again do not follow a power law and are qualitatively similar to the full curvature PDF.

To give a plausible explanation for the differences in likelihood of low-curvature events in the different directions, we connect large-scale, i.e. velocity, statistics with curvature vector statistics for and across all datasets. Considering the velocity PDFs, we can see a correlation between sub- or super-Gaussian tails for the PDFs of the velocity components and the PDFs of the curvature components. For the von Kármán flow, the PDFs of the  $x$ - and  $z$ -velocity component are approximately Gaussian while the PDF of the  $y$ -component has super-Gaussian tails. That is, the velocity fluctuates more strongly in  $y$ -

direction compared to the remaining two directions. For a higher probability of high-velocity events in one, here  $y$ -, direction we correspondingly observe a higher probability of small curvature values for the  $x$ - and  $z$ -component, compared to the  $y$ -component. For the RBC datasets, we have a reversed situation that allows the same interpretation. At  $Ra = 5.3 \cdot 10^8$ , the PDFs of the  $y$ - and  $z$ -component of the velocity are sub-Gaussian, the  $x$ -component is approximately Gaussian. That is, less high-speed events occur in the  $y$ - and  $z$ -direction compared to the  $x$ -direction. Correspondingly, we observe a lower probability of small curvature values in  $x$ -direction compared to the  $y$ - and  $z$ -direction and an increase of high curvature events. Similarly, at  $Ra = 1.53 \cdot 10^9$ , the  $u_z$  PDF has sub-Gaussian tail while the PDFs of  $u_x$  and  $u_y$  are approximately Gaussian. Again, we observe less curved trajectories in  $z$ -direction compared to the  $y$ - and  $x$ -direction with a higher probability of small curvature values in  $z$ -direction. For the boundary layer, the PDFs of all velocity components have sub-Gaussian tails. Here, the effect of the mean velocity in  $x$ -direction leads to a higher probability of small curvature values and a lower probability of high-curvature events in  $x$ -direction compared to the  $y$ - and  $z$ -direction. In a geometric sense, that means it is more likely to have meandering trajectories rather than helical trajectories in  $x$ -direction, that is, trajectories with no negative  $x$ -velocity.

Comparing all datasets, we point out that the differences between the low-curvature plateaux in the PDFs for von Kármán flow and bulk Rayleigh-Bénard convection shown in the insets of figs. 14 a), c) and d), respectively, are all of the same order of magnitude. Interestingly, according to the curvature vector statistics von Kármán flow is geometrically less isotropic than Rayleigh-Bénard convection in the bulk. For the latter, anisotropy – in the sense of differences between the statistics of the curvature vector components – decreases with increasing  $Ra$ , as can be expected.

Generally speaking, strong velocity events in one direction lead to an increase of low curvature events and a decrease of high-curvature events in that same direction. Based on the data of the turbulent ZPG boundary layer, we expect that a mean flow in one direction suppresses effects of extreme events on the curvature vector, especially for its component in stream-wise direction. This poses the question as to the effect of extreme acceleration events. It is conceivable that more extreme fluctuations at small scale in one direction leads to an increased probability of high curvature events in that direction. This would be physically intuitive as extreme events indicate turbulence, hence vortices, where trajectories are expected to be more curved, but this remains to be investigated.

## 6. Conclusions

Here, we compared Lagrangian statistics for four experimental datasets of three different types of turbulent flows, focusing on the effect large-scale motion has on the geometry of tracer particle trajectories. To observe and quantify the latter, we introduced the curvature vector and calculated statistics of its projections in the spatial directions determined by the experimental apparatus.

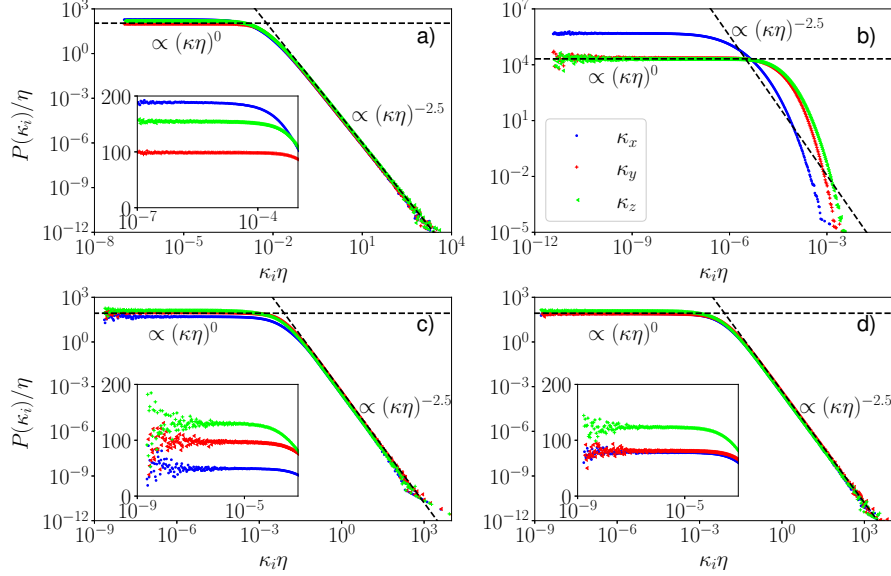


Figure 14: PDFs of the non-dimensionalised components of the curvature vector for different datasets in log-log representation, a) von Kármán flow b) Boundary layer, c) RBC I ( $Ra = 5.3 \cdot 10^8$ ), d) RBC II ( $Ra = 1.53 \cdot 10^9$ ). References lines  $(\kappa\eta)^0$  and  $(\kappa\eta)^{-2.5}$  are shown for all cases. In a), c), d) insets show PDFs in logarithmic-linear representation.

The datasets we considered were von Kármán flow, Rayleigh-Bénard convection in the bulk at two different Rayleigh numbers and a turbulent zero-pressure-gradient boundary layer in the logarithmic region. The Taylor-scale Reynolds numbers are  $Re_\lambda = 270$  for the von Kármán flow,  $Re_\lambda = 146$  and  $183$  for the RBC with  $Ra = 5.3 \cdot 10^8$  and  $Ra = 1.53 \cdot 10^9$  respectively and  $Re_\tau = 2295$  ( $Re_\lambda = 30$ ) for the turbulent boundary layer. To establish the baseline statistical characteristics of the flows, we first calculated PDFs of instantaneous velocity, acceleration, curvature and torsion of Lagrangian trajectories. Rayleigh-Bénard convection (bulk only) and von Kármán data behave statistically very similar: the PDFs of the velocity components are approximately Gaussian, acceleration PDFs have the expected wide tails. The power laws found for the tails of the curvature PDFs agree with previous results from numerical simulations of homogeneous and isotropic turbulence (HIT) [15], experiments of von Kármán flow [16] and numerical simulations of Rayleigh-Bénard convection [18]. Similarly, the torsion PDFs in all three datasets show the same scaling as for numerical simulations of homogeneous isotropic turbulence [17] and RBC [18]. Both curvature and torsion PDFs can be re-scaled using Heisenberg-Yaglom scaling to adjust for different Reynolds numbers and collapse onto a master curve. That is, the geometry and flow type do not seem to have an influence of any of these statistics, as long as there is no mean flow. The turbulent boundary layer has a mean flow in  $x$ -direction. The PDFs of all velocity components are



non-Gaussian, with approximately zero mean on wall-normal and span-wise directions. The acceleration PDFs do not seem to be influenced by that, we found PDFs with wide tails, which, when normalised by the respective standard deviations, collapsed into one. The curvature PDF has the same tail for small values of the curvature but deviates from the  $-2.5$  power law for high values. This is most likely due to the strong unidirectional flow suppressing high-curvature events and a strong unidirectional flow breaks the apparent universal form of the curvature PDF. The torsion PDF is unaffected by the geometry and the same power laws tails as for homogeneous isotropic turbulence are found.

For the components of the curvature vector, however, we observe marked differences between datasets and spatial directions. Firstly, the projection of the curvature vector is much more likely to be smaller in stream-wise direction compared to the span-wise and wall-normal direction for the ZPG boundary layer, reflecting the physical intuition that trajectories of particles with strong stream-wise velocity are less curved against the flow and more likely to meander in wall-normal and span-wise directions. Secondly, also for von Kármán flow and Rayleigh-Benard convection we find differences in the low-curvature tails of the curvature vector PDFs in the respective spatial directions. A comparison between velocity statistics and curvature vector statistics reveals that low-curvature events occur mostly in directions where velocity fluctuations are stronger. This is commensurate with the observations made for the turbulent boundary layer.

In summary, through connecting the statistics of the curvature vector with that of velocity fluctuations we demonstrate that large-scale motion in a given spatial direction results in meandering rather than helical trajectories. For the turbulent boundary layer, this is commensurate with the current understanding of superstructures [4, 50]. However, further analysis is required to distinguish between trajectories within a superstructure and the background. This requires the calculation of curvature statistics conditioned on the presence of a large-scale coherent structure, which in turn require a clear identification thereof. For RBC, turbulent superstructures can be found by data-driven means [8, 51], hence RBC lends itself well for a first investigation and quantification of the effects of turbulent superstructures on the geometry of tracer particle trajectories. Further work should also include a quantification of the observations made here through e.g. the calculation of joint statistics of velocity and curvature vector components, and specifically for RBC the detection of potential correlations with between high-curvature events and ejecting plumes [44]. The latter requires statistics conditioned on temperature. Finally, regarding the connection between Eulerian and Lagrangian statistics, one may try to connect curvature vector statistics with vortical structures. We will address these questions in future projects.

## Acknowledgements

This project was inspired by Bruno Eckhardt’s interest in curvature and torsion of tracer particle trajectories. Sadly, he passed away on August 7th

2019, and we do not know which research direction he would have pursued. We thank Michael Wilczek and Lukas Bentkamp for helpful discussions. Computational resources on Cirrus ([www.cirrus.ac.uk](http://www.cirrus.ac.uk)) have been obtained through Scottish Academic Access. This work received funding from Priority Programme SPP 1881 “Turbulent Superstructures” of the Deutsche Forschungsgemeinschaft (DFG, grant numbers LI3694/1, KA1808/21, BO5544/1 and SCHR1165/5). Yasmin Hengster was also supported by MAC-MIGS Centre for Doctoral training at the University of Edinburgh and Heriot-Watt University through EPSRC grant EP/S023291/1. We acknowledge funding from the European High-Performance Infrastructures in Turbulence (EuHIT) consortium for the DTrack measurement campaign at the von Kármán flow facility GTF3 and the support of the staff at MPIDS in Göttingen, in particular Eberhard Bodenschatz.

## References

- [1] K. C. Kim and R. J. Adrian. Very large-scale motion in the outer layer. *Phys. Fluids*, 11(2):417–422, 1999.
- [2] R. J. Adrian, C. D. Meinhart, and C. D. Tomkins. Vortex organization in the outer region of the turbulent boundary layer. *J. Fluid Mech.*, 422:1–54, 2000.
- [3] M. Guala, S. Hommema, and R. Adrian. Large-scale and very-large-scale motions in turbulent pipe flow. *J. Fluid Mech.*, 554:521 – 542, 05 2006.
- [4] N. Hutchins and I. Marusic. Evidence of very long meandering features in the logarithmic region of turbulent boundary layers. *J. Fluid Mech.*, 579:1 – 28, 2007.
- [5] N. Hutchins, K. Chauhan, I. Marusic, J. Monty, and J. Klewicki. Towards Reconciling the Large-Scale Structure of Turbulent Boundary Layers in the Atmosphere and Laboratory. *Bound.-Layer Meteorol.*, 145(2):273–306, 2012.
- [6] A. Pandey, J. Scheel, and J. Schumacher. Turbulent superstructures in Rayleigh-Bénard convection. *Nat. Commun.*, 9:2118, 2018.
- [7] R. J. A. M. Stevens, A. Blass, X. Zhu, R. Verzicco, and D. Lohse. Turbulent thermal superstructures in Rayleigh-Bénard convection. *Phys. Rev. Fluids*, 3:041501, 2018.
- [8] C. Schneide, A. Pandey, K. Padberg-Gehle, and J. Schumacher. Probing turbulent superstructures in Rayleigh-Bénard convection by Lagrangian trajectory clusters. *Phys. Rev. Fluids*, 3:113501, 2018.
- [9] D. Krug, D. Lohse, and R. J. A. M. Stevens. Coherence of temperature and velocity superstructures in turbulent Rayleigh-Bénard flow. *J. Fluid Mech.*, 887:A2, 2020.

- [10] J. P. Monty, J. A. Stewart, R. C. Williams, and M. S. Chong. Large-scale features in turbulent pipe and channel flows. *J. Fluid Mech.*, 589:147–156, 2007.
- [11] N. Hutchins, J.P. Monty, B. Ganapathisubramani, H.C.H. Ng, and I. Marusic. Three-dimensional conditional structure of a high-Reynolds-number turbulent boundary layer. *J. Fluid Mech.*, 673:255–285, 2011.
- [12] B. Ganapathisubramani and E. Longmire. Characteristics of vortex packets in turbulent boundary layers. *J. Fluid Mech.*, 478:35 – 46, 2003.
- [13] N. Hutchins and I. Marusic. Large-scale influences in near-wall turbulence. *Philos. Trans. Royal Soc. A*, 365(1852):647–664, 2007.
- [14] M. Bross, T. Fuchs, and C. J. Kähler. Interaction of coherent flow structures in adverse pressure gradient turbulent boundary layers. *J. Fluid Mech.*, 873:287–321, 2019.
- [15] W. Braun, F. De Lillo, and B. Eckhardt. Geometry of particle paths in turbulent flows. *J. Turbul.*, 7:N62, 2006.
- [16] H. Xu, N. Ouellette, and E. Bodenschatz. Curvature of Lagrangian Trajectories in Turbulence. *Phys. Rev. Lett.*, 98:050201, 2007.
- [17] A. Scagliarini. Geometric properties of particle trajectories in turbulent flows. *J. Turbul.*, 12:N25, 2011.
- [18] K. M. J. Alards, H. Rajaei, L. Del Castello, R. P. J. Kunnen, F. Toschi, and H. J. H. Clercx. Geometry of tracer trajectories in rotating turbulent flows. *Phys. Rev. Fluids*, 2:044601, 2017.
- [19] S. Gesemann, F. Huhn, D. Schanz, and A. Schröder. From Particle Tracks to Velocity and Acceleration Fields Using B-Splines and Penalties. *Proceedings of 18th International Symposium on Applications of Laser Techniques to Fluid Mechanics*, July 4-7, 2016. Lisbon, Portugal.
- [20] D. Schanz, S. Gesemann, and A. Schröder. Shake-The-Box: Lagrangian particle tracking at high particle image densities. *Exp. Fluids*, 57(5):70, 2016.
- [21] A. Schröder and D. Schanz. 3D Lagrangian Particle Tracking in Fluid Mechanics. *Annu. Rev. Fluid Mech.*, 55(1):511–540, 2023.
- [22] B. Wieneke. Iterative reconstruction of volumetric particle distribution. *Meas. Sci. Technol.*, 24(2):024008, 2012.
- [23] T. Jahn, D. Schanz, and A. Schröder. Advanced iterative particle reconstruction for Lagrangian particle tracking. *Exp. Fluids*, 62(8):179, 2021.

- [24] A. Schröder, D. Schanz, S. Gesemann, F. Huhn, T. Buchwald, D. Garaboa Paz, and E. Bodenschatz. Measurements of the energy dissipation rate in homogeneous turbulence using dense 3D Lagrangian Particle Tracking and FlowFit. *Proceedings of 20th International Symposium on Application of Laser and Imaging Techniques to Fluid Mechanics*, July 11-14, 2022. Lisbon, Portugal.
- [25] J. Bosbach, D. Schanz, P. Godbersen, and A. Schröder. Spatially and temporally resolved measurements of turbulent Rayleigh-Bénard convection by Lagrangian particle tracking of long-lived helium-filled soap bubbles. *Proceedings of 14th International Symposium on Particle Image Velocimetry - ISPIV 2021*, August 1-5, 2021. Munich, Germany.
- [26] P. Godbersen, J. Bosbach, D. Schanz, and A. Schröder. Beauty of turbulent convection: A particle tracking endeavor. *Phys. Rev. Fluids*, 6:110509, 2021.
- [27] D. Schanz, A. Schröder, M. Novara, R. Geisler, J. Agocs, F. Eich, M. Bross, and C. J. Kähler. Large-scale volumetric characterization of a turbulent boundary layer flow. *Proceedings of the 13th International Symposium on Particle Image Velocimetry – ISPIV 2019*, July 22-24, 2019. Munich, Germany.
- [28] N. Mordant, A. Crawford, and E. Bodenschatz. Three-Dimensional Structure of the Lagrangian Acceleration in Turbulent Flows. *Phys. Rev. Lett.*, 93:214501, 2004.
- [29] P. K. Yeung and S. B. Pope. Lagrangian statistics from direct numerical simulations of isotropic turbulence. *J. Fluid Mech.*, 207:531–586, 1989.
- [30] R. Ni, SD. Huang, and KQ. Xia. Lagrangian acceleration measurements in convective thermal turbulence. *J. Fluid Mech.*, 692:395–419, 2012.
- [31] N. Stelzenmuller, J. I. Polanco, L. Vignal, I. Vinkovic, and N. Mordant. Lagrangian acceleration statistics in a turbulent channel flow. *Phys. Rev. Fluids*, 2:054602, 2017.
- [32] A. A. Townsend. The measurement of double and triple correlation derivatives in isotropic turbulence. *Math. Proc. Camb. Philos. Soc.*, 43(4): 560–570, 1947.
- [33] G. K. Batchelor. *The Theory of Homogeneous Turbulence*. Cambridge University Press, 1953.
- [34] N. T. Ouellette, H. Xu, M. Bourgoïn, and E. Bodenschatz. Small-scale anisotropy in Lagrangian turbulence. *New J. Phys.*, 8(6):102, 2006.
- [35] G. A. Voth, A. La Porta, A. Crawford, E. Bodenschatz, and J. Alexander. Measurement of particle accelerations in fully developed turbulence. *J. Fluid Mech.*, 469:121–160, 2002.

- [36] L. Bentkamp, C. C. Lalescu, and M. Wilczek. Persistent accelerations disentangle Lagrangian turbulence. *Nat. Commun.*, 10:3550, 2019.
- [37] L. Biferale, G. Boffetta, A. Celani, B. Devenish, A. Lanotte, and F. Toschi. Multifractal Statistics of Lagrangian Velocity and Acceleration in Turbulence. *Phys. Rev. Lett.*, 93:064502, 2004.
- [38] J. M. Lawson, E. Bodenschatz, C. C. Lalescu, and M. Wilczek. Bias in particle tracking acceleration measurement. *Exp. Fluids*, 59(11):172, 2018.
- [39] N. Mordant, E. L  v  que, and JF. Pinton. Experimental and numerical study of the Lagrangian dynamics of high Reynolds turbulence. *New J. Phys.*, 6(1):116, 2004.
- [40] A. La Porta, G. A. Voth, A. Crawford, J. Alexander, and E. Bodenschatz. Fluid particle accelerations in fully developed turbulence. *Nature*, 409:1017–1019, 2001.
- [41] C. C. Lalescu and M. Wilczek. Acceleration statistics of tracer particles in filtered turbulent fields. *J. Fluid Mech.*, 847:R2, 2018.
- [42] Y. Hengster and M. Linkmann. Lagrangian curvature statistics from Gaussian subensembles in turbulence. *in preparation*, 2023.
- [43] L. Biferale and F. Toschi. Joint statistics of acceleration and vorticity in fully developed turbulence. *J. Turbul.*, 6:N40, 2005.
- [44] J. Schumacher. Lagrangian studies in convective turbulence. *Phys. Rev. E*, 79:056301, 2009.
- [45] M. Bross, D. Schanz, M. Novara, F. Eich, A. Schr  der, and C.J. K  hler. Turbulent superstructure statistics in a turbulent boundary layer with pressure gradients. *Eur. J. Mech. B Fluids*, 2023. under review.
- [46] A. N. Kolmogorov. Dissipation of Energy in Locally Isotropic Turbulence. *Akademiia Nauk SSSR Doklady*, 32:16, 1941.
- [47] A. N. Kolmogorov. The Local Structure of Turbulence in Incompressible Viscous Fluid for Very Large Reynolds’ Numbers. *Akademiia Nauk SSSR Doklady*, 30:301–305, 1941.
- [48] W. Heisenberg. Zur statistischen Theorie der Turbulenz. *Zeitschrift f  r Physik*, 124:628–657, 1948.
- [49] A. M. Yaglom. On the acceleration field in a turbulent flow. *C. R. Akad. URSS*, 67(5):795–798, 1949.
- [50] K. Kevin, J. Monty, and N. Hutchins. The meandering behaviour of large-scale structures in turbulent boundary layers. *J. Fluid Mech.*, 865:R1, 2019.
- [51] P. P. Vieweg, C. Schneide, K. Padberg-Gehle, and J. Schumacher. Lagrangian heat transport in turbulent three-dimensional convection. *Phys. Rev. Fluids*, 6:L041501, 2021.